INVITED PAPER *Special Section on Technologies and Proof-of-Concept Activities for 5G Advanced and 6G*

# Smart Radio Environments with Intelligent Reflecting Surfaces for 6G Sub-Terahertz-Band Communications

**Yasutaka OGAWA**[†], ***Fellow***, **Shuto TADOKORO**[†], ***Nonmember***, **Satoshi SUYAMA**[††], ***Senior Member***, **Masashi IWABUCHI**[†††], ***Member***, **Toshihiko NISHIMURA**[†a)], ***Senior Member***, **Takanori SATO**[†], **Junichiro HAGIWARA**[†], ***Members***, ***and*** **Takeo OHGANE**[†], ***Fellow***

**SUMMARY** Technology for sixth-generation (6G) mobile communication system is now being widely studied. A sub-Terahertz band is expected to play a great role in 6G to enable extremely high data-rate transmission. This paper has two goals. (1) Introduction of 6G concept and propagation characteristics of sub-Terahertz-band radio waves. (2) Performance evaluation of intelligent reflecting surfaces (IRSs) based on beamforming in a sub-Terahertz band for smart radio environments (SREs). We briefly review research on SREs with reconfigurable intelligent surfaces (RISs), and describe requirements and key features of 6G with a sub-Terahertz band. After that, we explain propagation characteristics of sub-Terahertz band radio waves. Important feature is that the number of multipath components is small in a sub-Terahertz band in indoor office environments. This leads to an IRS control method based on beamforming because the number of radio waves out of the optimum beam is very small and power that is not used for transmission from the IRS to user equipment (UE) is little in the environments. We use beams generated by a Butler matrix or a DFT matrix. In simulations, we compare the received power at a UE with that of the upper bound value. Simulation results show that the proposed method reveals good performance in the sense that the received power is not so lower than the upper bound value.

***key words:*** *6G mobile communications, sub-Terahertz band, smart radio environment, intelligent reflecting surface*

## 1. Introduction

Network services in fifth-generation (5G) mobile communication system have already started in many countries, and techniques for sixth generation (6G) mobile communication system are now being extensively studied in industry and academia [1]–[5]. 6G requires extremely high data-rate communication over 100 Gbps, which is much above that in 5G, about 10 Gbps. To support such high data rates, we need a Terahertz band above 100 GHz where an extremely wide bandwidth is available. Many studies have been done on this field [6]–[9]. A frequency range of 100–300 GHz will be used in 6G, and the spectrum is called a sub-Terahertz band [9]. To overcome large propagation losses in the band, we use a high-gain directional antenna, which is realized by an array composed of many elements. In addition, radio waves in a sub-Terahertz band are hard to propagate behind an obstacle due to large diffraction losses. Studies to alter such propagation environments to smart radio environments (SREs) have been attracting much attention for 6G. SREs are realized by using intelligent reflecting surfaces (IRSs) or more generally reconfigurable intelligent surfaces (RISs) [10].

Against this background, this paper has two goals:

1. Introduction of 6G concept and propagation characteristics of sub-Terahertz-band radio waves
2. Performance evaluation of IRSs based on beamforming in a sub-Terahertz band for SREs

Here, we briefly review SREs with RISs. Figure 1(a) shows the block diagram of a conventional wireless communication system where we optimize the transmitter and receiver depending on the radio environment. In the system, the environment cannot be controlled but can only be adapted to. However, wireless researchers have recently noticed that it is possible to program radio environments as shown in Fig. 1(b). Using RISs, we can control characteristics of radio waves such as reflection (beamforming),

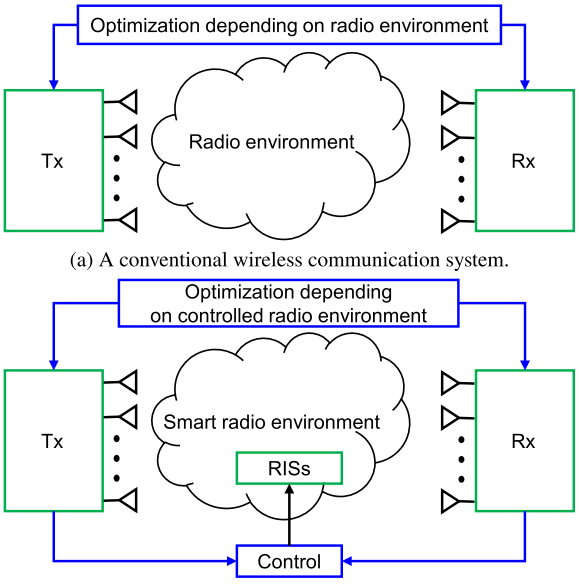


(a) A conventional wireless communication system.

(b) A wireless communication system in SRE.

**Fig. 1** Wireless communication systems.

Manuscript received January 12, 2023.
Manuscript revised February 14, 2023.
Manuscript publicized May 23, 2023.

[†]The authors are with the Faculty/Graduate School of Information Science and Technology, Hokkaido University, Sapporo-shi, 060-0814 Japan.
[††]The author is with NTT DOCOMO, INC., Yokosuka-shi, 239-8536 Japan.
[†††]The author is with NTT Access Network Service Systems Laboratories, Nippon Telegraph and Telephone Corporation, Yokosuka-shi, 239-0847 Japan.
a) E-mail: nishim@ist.hokudai.ac.jp

DOI: 10.1587/transcom.2022FGI0002

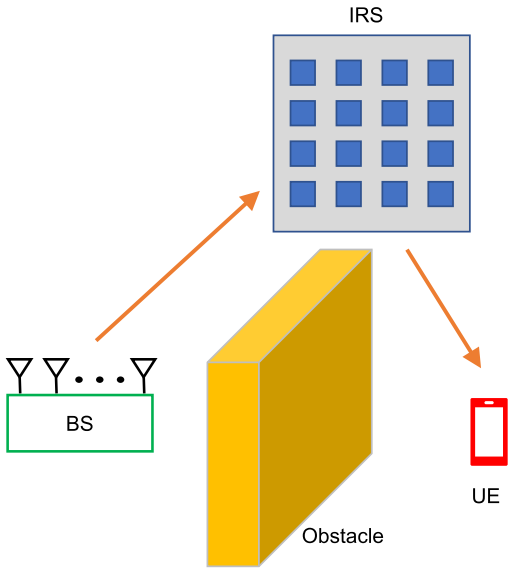


**Fig. 2** An example of RIS-assisted use case (IRS).

refraction, absorption. Deploying RISs in a network, we can turn the environment into a smart reconfigurable space. This is the concept of SREs.

Several survey papers on SREs and RISs have been published during these few years [10]–[19]. The article [18] presents an industrial viewpoint as well as the progress on research and standardization on RISs. Furthermore, prototypes of RISs have been experimentally studied [20]–[22].

Here, we consider a typical use case of RISs, and state its two challenges. As shown in Fig. 2, user equipment (UE) is in a non-line-of-sight (NLOS) environment because the direct path from a base station (BS) is blocked by an obstacle. An RIS consisting of reflecting elements is placed at the position where both of the BS-to-RIS and RIS-to-UE channels are in line-of-sight (LOS) cases. The reflecting elements are connected to phase-shift devices which can adjust the phases of the impinging radio waves. In this use case, the RIS is called an IRS. If the phase-shift devices are controlled adequately, the reflected radio waves are steered toward the UE. We assume that the IRS does not have either receivers or transmitters for sub-Terahertz-band radio waves, and therefore they are a passive beamformer. This is the reason why IRSs have lower hardware cost and energy consumption. A typical approach to controlling the phase-shift devices is to perform two processes: channel estimation and phase optimization based on the estimated channels. In this method, as seen from Fig. 2, we need to estimate the channels between the BS and IRS, and also the channels between the IRS and UE. Since the IRS has many reflecting elements, the number of channels is large. Furthermore, the IRS does not have receivers, but only reflects impinging radio waves changing the phases. Many channel estimation algorithms are introduced in [10], but the estimation is still a difficult issue in wireless systems with IRSs. Once the channels are available, we optimize the phases. Unfortunately, the problem is non-convex and difficult to solve [23]. We need to obtain a suboptimal solution. The Ref. [10] reviews many algorithms to tackle this problem.

Moreover, to apply RIS in the future, RIS may be exploited to realize a new massive MIMO transceiver architecture in high frequency bands. It is a method to construct an equivalently extremely large-scale massive MIMO transceiver by beamforming modulated signal with a transceiver which consists of a small array antenna or a lens antenna and then applying the generated beam to a large RIS that transmits or reflects it. By properly performing two-stage beam control, it is possible to ensure a large beamforming gain or to dynamically change the function and its capability to increase the number of spatially multiplexed MIMO streams [24]. For example, mounting the large RIS all over the wall of a building can realize the extremely large-scale massive MIMO transceiver at low cost, which could not be realized by conventional construction methods.

In this paper, we investigate IRS control based on beamforming. An IRS has a set of beams. A BS sends pilot symbols, and for a different pilot, the IRS changes the beam. A UE measures the received power for each beam, and informs the BS of the beam which provides the largest received power. The BS controls the IRS in such a way that it uses the optimum beam providing the maximum power at the UE. The idea does not need either channel state information or phase optimization. It is easy to determine the phases of the IRS. However, the performance depends on environments where it is deployed. When we have only a few multipath components in the environment, the method will work very well because the beam along a dominant multipath component provides large power. The IRSs based on beamforming have been reported so far in references including [21], [25]. The frequencies treated in these papers are 5.8 GHz and millimeter-wave bands, respectively. Unfortunately, the performance has not been examined using a reliable sub-Terahertz-band channel model.

Recently, sub-Terahertz-band transmission measurements have been carried out [26]–[29]. According to [27], the total number of observed multipaths at 140 GHz is much smaller than the number at 28 GHz in office environments. It is expected that the IRSs based on beamforming work well in sub-Terahertz bands. In this paper, we evaluate the performance using the sub-Terahertz-band channel model proposed in [27]. Such evaluation has not been done so far, and this is the original part for the second goal of this paper.

The rest of the paper is organized as follows. In Sect. 2, we briefly review 6G utilizing sub-Terahertz band radio waves. In Sect. 3, we show measurement results and the channel model for sub-Terahertz-band radio waves. Sect. 4 states the IRS control based on beamforming and its performance using the sub-Terahertz-band characteristics. Finally, we conclude the paper in Sect. 5.

## 2. Utilization of Sub-Terahertz Band for 6G

At present, with popularization of big data and artificial intelligence (AI), a cyber-physical system (CPS) has been

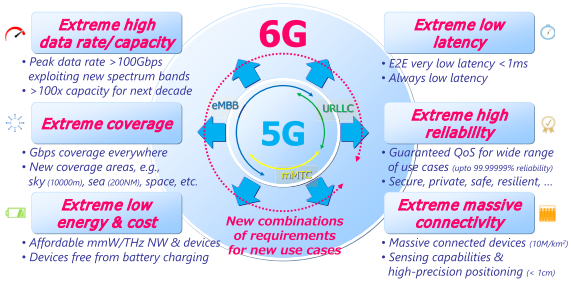


**Fig. 3** NTT DOCOMO's view on requirements for 6G [31].

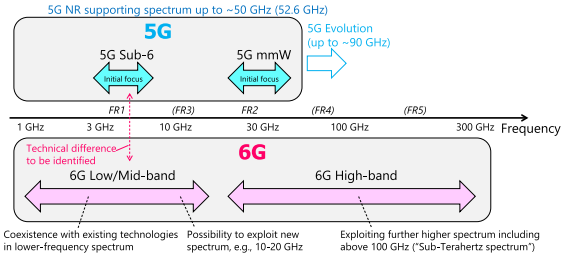


**Fig. 4** Spectrum extension for 6G [31].

attracting much attention. AI reproduces the real world in cyber space and emulates it beyond the constraints of the real world, so that future prediction and new knowledge can be discovered. A role of mobile communications in CPS is assumed to provide high-capacity and low-latency transmission of images, videos, and sensing information from the real world and feedback/actuate to the real world through high-reliability and low-latency control signaling. Therefore, to realize an advanced CPS in the 2030s, 6G with extreme performance is needed.

NTT DOCOMO (hereafter, DOCOMO) has already released the first version of white paper for 5G Evolution and 6G in January 2020 [30], and then the white paper has been updated as revision 5.0 based on the further studies in November 2022 [31]. As mentioned before, 6G is an innovative infrastructure to support future society and industry in the 2030s and aims to provide required extreme performance. Figure 3 shows DOCOMO's view on requirements for 6G [31]. They consist of six components such as extreme high data rate and capacity, extreme coverage, extreme low energy and cost, extreme low latency, extreme high reliability, and extreme massive connectivity. Especially, it is expected that extreme high-data-rate communication exceeding 100 Gbps will be provided and that new sensory services such as "multi-sensory communication" that are equal to or exceed the sensory quality of the actual senses can be actualized by the extreme high-data-rate 6G. Hence, promising 6G use cases are human augmentation, BrainTech, and transmission of emotions, which may trigger a major paradigm shift in the value-add provided by communication services [31]. Furthermore, in the extreme massive connectivity of the 6G requirements, 6G should support ten million devices per square km. The mobile communication network itself is also expected to evolve to have functions for sensing the real world such as high-precise positioning with the error of a centimeter or less and object detection around the mobile devices by using radio waves. In addition to AI, such capabilities of the wireless sensing and the high-precision positioning are very useful to optimize DOCOMO's proposed "New Radio Network Topology (NRNT)" including SREs with IRSs in 6G [31]. NRNT is a technical concept for 5G Evolution and 6G. The technical components to configure NRNT include distributed MIMO, wireless relay/repeater and RIS/IRS. Since the IRS can control the reflected wave according to user mobility, it is expected to improve or extend coverage at low cost. From the viewpoint of mobile operators, in addition to the coverage expansion, it is important to improve system capacity. IRS may improve the number of MIMO streams by newly generating LOS paths. Note that technical issues related to NRNT are summarized in [32].

As shown in Fig. 4, 5G supports frequency bands up to 52.6 GHz and it is considered that the frequency bands will be extended up to almost 90 GHz in the future. Toward 6G, the Federal Communications Commission (FCC) in the United States announced to open new frequency bands between 95 GHz and 3 THz for experimental trials. In order to provide extreme high-data-rate 6G communications over 100 Gbps, sub-Terahertz bands should be exploited, because much wider bandwidth is available compared with 5G.

However, to utilize the sub-Terahertz band in 6G, as was the case with the introduction of the millimeter-wave band in 5G, there are many technical issues that need to be resolved by the 2030s [31], [33]–[35]. The technical issues are diverse and mainly exist in four areas: radio propagation, radio frequency (RF) devices, modulation and demodulation schemes, and air interfaces, which are summarized in detail for each area in [34]. The sub-Terahertz waves have a fundamental technological problem that the radio waves do not fly far, because the rectilinearity and pathloss of the sub-Terahertz waves are higher than those of the conventional millimeter waves. Thus, measuring sub-Terahertz-band radio propagation characteristics in real environments and establishing channel models based on the measurement results, and high-precision propagation simulation methods suitable for the sub-Terahertz band are needed for 6G. In Sect. 3 of this paper, some examples of the measurement results of the sub-Terahertz propagation characteristics will be introduced in detail.

Focusing on the technical issues in the RF devices, characteristics of the RF devices mainly depend on frequency bands and signal bandwidths, and in addition to high performance and high integration of the RF devices supporting a massive MIMO transceiver, it is necessary to be able to manufacture semiconductor devices at a level of performance and cost that can be used in actual 6G commercial services of the 2030s. Vigorous development of the sub-Terahertz RF devices for 6G is underway all over the world. In Japan, one of the development projects is being carried out in research and development for expansion of radio wave resource commissioned by the Ministry of Internal Affairs and Communications (MIC). Some impairments of the RF devices such as

frequency selectivity, IQ imbalance, DC offset, carrier leak, phase noise, and nonlinear distortion may cause performance degradation in the sub-Terahertz 6G communications while these RF impairments can be partly compensated by digital signal processing [31], [33], [34]. A compensation method for nonlinear distortion of a transmitted single-carrier signal at the receiver side has been proposed in the sub-Terahertz band [36].

Considering the above technical issues of the sub-Terahertz radio propagation and the RF devices, 6G radio access technologies (RATs) including modulation and demodulation schemes and air interfaces should be designed. In [31], [33], DOCOMO's technical concept and view of sub-Terahertz 6G RATs have been already introduced. Moreover, link-level simulations of the sub-Terahertz 6G RATs to achieve over-100 Gbps downlink throughput have been conducted, and system performance of the 6G RATs through system-level simulations using multiple base stations and mobile stations have been also evaluated [35], [37]. In addition, some 6G experimental trials of the sub-Terahertz RATs are being prepared [38].

## 3. Sub-Terahertz-Band Propagation Characteristics and Channel Model

As seen from the above, sub-Terahertz-band propagation is crucial for 6G. In this section, we describe the propagation measurements conducted by DOCOMO and the channel model proposed by New York University. It will be shown that the number of multipath components in sub-Terahertz bands is small in indoor office environments. This feature is important for the IRS control, which will be described in Sect. 4.

### 3.1 Measurement of Sub-Terahertz-Band Propagation Characteristics in Indoor Conference Room

DOCOMO has measured radio propagation characteristics at 160 GHz and 300 GHz in indoor environments [39], and the measurement results have been submitted to ITU Radiocommunication (ITU-R) Working Party 5D (WP5D) through Beyond 5G Promotion Consortium's Beyond 5G white paper (version 1.51) [40].

Due to larger blocking loss of obstacles in the sub-Terahertz band, it is necessary to investigate methods to relax the severe blocking effect, such as utilizing reflected waves from walls and ceilings or artificially generated by IRSs. Thus, it is important to clarify both path loss and angle of arrival (AOA) of direct and reflected waves in the sub-Terahertz-band indoor environments. In this subsection, an example of 160 GHz-band measurement results of the path loss and AOA in an indoor conference room is introduced briefly [39]. As shown in Figs. 5(a) and (b), a measurement environment is the conference room surrounded by walls and glass windows on all sides in DOCOMO R&D Center. In the propagation measurement, a directional antenna for transmitter (Tx) and receiver (Rx) antennas was used.

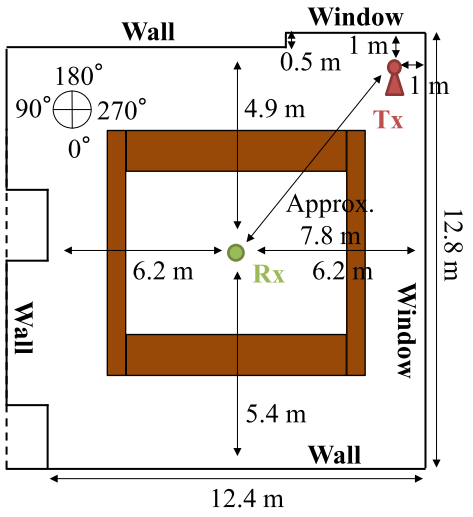


(a) Diagram of measurement environment.


(b) Photo of measurement environment.

**Fig. 5** Measurement environment.

**Table 1** Measurement parameters.

| | |
|---|---|
| Transmission signal | Continuous wave (CW) |
| Tx antenna | Horn antenna |
| Rx antenna | Cassegrain antenna |
| Tx azimuth HPBW | 18 deg. |
| Tx elevation HPBW | 17 deg. |
| Rx azimuth HPBW | 0.9 deg. |
| Rx elevation HPBW | 0.9 deg. |
| Tx antenna height | 3 m |
| Rx antenna height | 1 m |

Horizontal and vertical directions of the Tx antenna were changed every 10 degrees, and the Rx antenna was rotated by 360 degrees horizontally while changing the angle of elevation. Table 1 gives measurement parameters. The half power beam width (HPBW) of the Rx antenna is approximately 1 degree, and the pencil beam with the high gain was employed. Figure 6 shows the minimum path loss in all Tx antenna directions for each Rx antenna direction. A direct wave (shown in red) arrived with a path loss of almost 100 dB from the direction of approximately 230 degrees and 15 degrees, represented as (230, 15), in the horizontal and elevation angles, respectively. In addition, it is possible to confirm four arrival reflected waves referred to as A1, A2, A3, and A4 in the directions of approximately (40, 6), (110, 6), (230, 24), and (350, 6) in the horizontal and elevation angles, respectively. Note that the measurement results of path loss for A1, A2, A3, and A4 are approximately 106 dB,

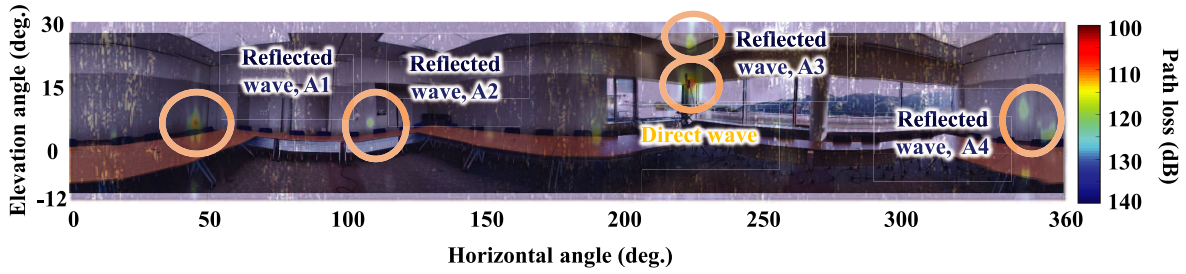


**Fig. 6** Measurement results of pathloss.

117 dB, 114 dB, and 121 dB, respectively, and in the measured conference room, only four dominant reflected waves from the walls and ceiling surrounding the Rx were observed in addition to the direct wave.

### 3.2 Channel Model Based on Measurements in an Office Building

In this subsection, we state a channel model for a sub-Terahertz band proposed by New York University. Ju et al. [27] has presented a channel model for millimeter-wave and sub-Terahertz bands based on propagation measurements at 28 and 140 GHz. The measurements were conducted for different Tx-Rx location pairs in a typical indoor office environment (65.5 m × 35 m × 2.7 m) with offices, conference rooms, classrooms, long hallways, open-plan cubicles, and elevators. The Tx-Rx distance ranged from 3.9 m to 45.9 m for 28 GHz and from 3.9 m to 39.2 m for 140 GHz. The channel model was derived from over 15,000 measured power delay profiles, and it uses the concept of time clusters (TCs) and subpaths (SPs) [41]. TCs are composed of multipath components traveling close in time. A SP is a multipath component via a TC. According to [27], the total number of multipath components at 140 GHz is much smaller than the number at 28 GHz, and that the 140 GHz channel is much sparser than the channel at 28 GHz. From Figs. 3, 4 and Table VII in the Ref. [27], we see the following:

1. The number of TCs of 140 GHz is equal to or less than 3 in all the LOS cases.
2. The number of SPs within a cluster is 1 or 2 in about 80 percent cases.
3. The total number of multipath components in the LOS environments is equal to or less than 5 in 7 cases out of 8 ones.

The proposed channel model is easy to use for simulations [42], and the performance of IRS is evaluated using it in the next section.

## 4. IRS Based on Beamforming

This section clarifies IRS control based on beamforming treated in this paper. After that, we show its performance using computer simulations.

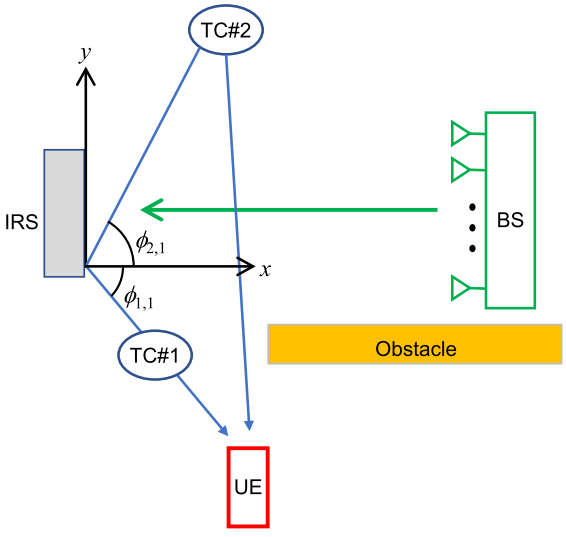


(a) Top view.

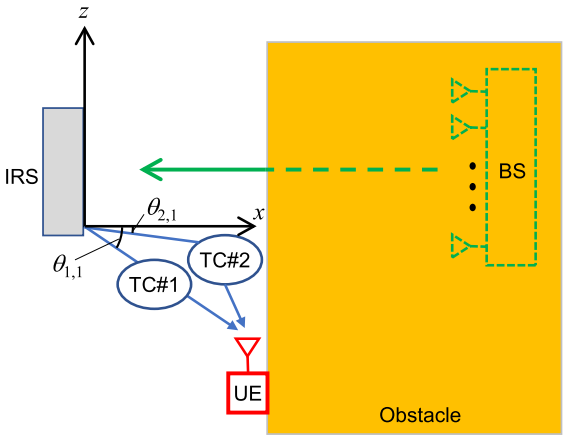


(b) Elevation view.

**Fig. 7** An IRS-assisted wireless network.

### 4.1 System Model and IRS Control

Figure 7 depicts a system model discussed here. Note that its multipath environment is an example. In the figure, we have two TCs and one SP per TC. We express azimuth and elevation angles as $\phi$ and $\theta$, respectively. The positive azimuth direction is counterclockwise with respect to the x-axis, and the azimuth angles of departure (AODs) $\phi_{1,1}$ and $\phi_{2,1}$ are

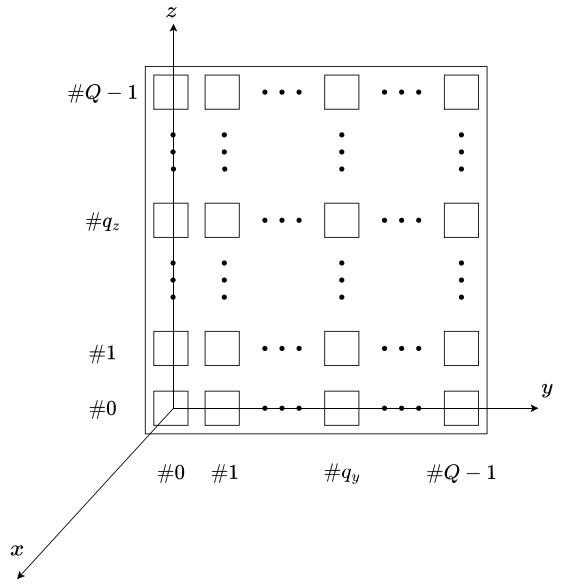


**Fig. 8** An IRS with $Q \times Q$ reflecting elements.

negative and positive, respectively. Since both of TC#1 and TC#2 are below the $x$-$y$ plane, the elevation angles of departure (EODs) $\theta_{1,1}$ and $\theta_{2,1}$ are negative. The direct path from the BS is blocked by an obstacle, and the UE is in a NLOS environment. The IRS reflects the incident radio waves toward the UE that has a single antenna. The IRS consists of $Q \times Q$ reflecting elements with half-wavelength spacing as shown in Fig. 8, where $Q$ is a power of 2. Since the BS knows the location of the IRS, it can transmit the radio waves exactly to the IRS. We assume that the BS antenna array is so large that the beam to the IRS is sharp and the direct signal alone reaches the IRS. We can ignore multipath components between the BS and IRS. Furthermore, for the sake of simplicity, we assume that the IRS is located straight in front of the BS. Then, the radio waves arrive at the reflecting elements in phase. This assumption can be easily removed by adjusting a phase-shift device at each reflecting element to compensate for the phase difference.

Here, we describe an IRS control method based on beamforming treated in this paper. We have four codebooks defined as follows:

1. Codebook BB consisting of $Q^2$ beams formed by phases of a Butler matrix for both the azimuth and the elevation directions
2. Codebook DB consisting of $Q^2$ beams formed by phases of a DFT matrix for the azimuth direction and phases of a Butler matrix for the elevation direction
3. Codebook BD consisting of $Q^2$ beams formed by phases of a Butler matrix for the azimuth direction and phases of a DFT matrix for the elevation direction
4. Codebook DD consisting of $Q^2$ beams formed by phases of a DFT matrix for both the azimuth and the elevation directions

The reason why we use the four codebooks will be clarified later. It should be noted that we do not have either Butler matrix circuits or DFT matrix circuits. Phases realized by those circuits are given to phase-shift devices. Concretely speaking, the phases of complex weights for beamforming stated below are given to the phase-shift devices of the IRS.

Here, we derive the beam patterns for the above codebooks. We assume that the incident power to the IRS is reflected without attenuation or amplification. As for reflecting radio waves to the UE, we consider that the IRS works equivalently as a phased array with isotropic antenna elements, and that the input power to the phased array is the incident power to the IRS. From these assumptions, the complex weight for Codebook BB is given by

$$\begin{aligned} & w_{\mathrm{BB},p_a,p_e,q_y,q_z} \\ &= \frac{1}{Q} \exp\left\{\frac{-j\pi q_y\,(-Q+2p_a+1)}{Q}\right\} \\ &\quad \times \exp\left\{\frac{-j\pi q_z\,(-Q+2p_e+1)}{Q}\right\} \end{aligned} \tag{1}$$

where

$$p_a = 0, 1, \ldots, Q-1 \tag{2}$$
$$p_e = 0, 1, \ldots, Q-1 \tag{3}$$
$$q_y = 0, 1, \ldots, Q-1 \tag{4}$$
$$q_z = 0, 1, \ldots, Q-1 \tag{5}$$

The complex weight excites the element $(q_y,\ q_z)$ to form the beam for $p_a$th in the azimuth direction and $p_e$th in the elevation direction. The coefficient $1/Q$ in (1) is introduced to make the radiated power from the phased array equal to the input power. The beam pattern for Codebook BB is derived as follows:

$$\begin{aligned} & g_{\mathrm{BB},p_a,p_e}(\phi,\theta) \\ &= \sum_{q_y=0}^{Q-1}\sum_{q_z=0}^{Q-1} w_{\mathrm{BB},p_a,p_e,q_y,q_z} \\ &\quad \times \exp\left\{j\pi\left(q_y\cos\theta\sin\phi + q_z\sin\theta\right)\right\} \\ &= \frac{1}{Q}\frac{\sin\left\{\frac{\pi Q}{2}\left(\cos\theta\sin\phi+1-\frac{2p_a}{Q}-\frac{1}{Q}\right)\right\}}{\sin\left\{\frac{\pi}{2}\left(\cos\theta\sin\phi+1-\frac{2p_a}{Q}-\frac{1}{Q}\right)\right\}} \\ &\quad \times \frac{\sin\left\{\frac{\pi Q}{2}\left(\sin\theta+1-\frac{2p_e}{Q}-\frac{1}{Q}\right)\right\}}{\sin\left\{\frac{\pi}{2}\left(\sin\theta+1-\frac{2p_e}{Q}-\frac{1}{Q}\right)\right\}} \\ &\quad \times \exp\left\{j\,(Q-1)\,\frac{B_{p_a}+B_{p_e}}{2}\right\} \end{aligned} \tag{6}$$

where

$$B_{p_a} = \pi\left(\cos\theta\sin\phi+1-\frac{2p_a}{Q}-\frac{1}{Q}\right) \tag{7}$$

$$B_{p_e} = \pi\left(\sin\theta + 1 - \frac{2p_e}{Q} - \frac{1}{Q}\right) \tag{8}$$

Similarly, the complex weights for Codebooks DB, BD, DD are expressed as

$$\begin{aligned} &w_{\mathrm{DB},p_a,p_e,q_y,q_z} \\ &= \frac{1}{Q}\exp\left\{\frac{-j\pi q_y\left(-Q+2p_a+2\right)}{Q}\right\} \\ &\quad\times\exp\left\{\frac{-j\pi q_z\left(-Q+2p_e+1\right)}{Q}\right\} \end{aligned} \tag{9}$$

$$\begin{aligned} &w_{\mathrm{BD},p_a,p_e,q_y,q_z} \\ &= \frac{1}{Q}\exp\left\{\frac{-j\pi q_y\left(-Q+2p_a+1\right)}{Q}\right\} \\ &\quad\times\exp\left\{\frac{-j\pi q_z\left(-Q+2p_e+2\right)}{Q}\right\} \end{aligned} \tag{10}$$

$$\begin{aligned} &w_{\mathrm{DD},p_a,p_e,q_y,q_z} \\ &= \frac{1}{Q}\exp\left\{\frac{-j\pi q_y\left(-Q+2p_a+2\right)}{Q}\right\} \\ &\quad\times\exp\left\{\frac{-j\pi q_z\left(-Q+2p_e+2\right)}{Q}\right\} \end{aligned} \tag{11}$$

From (9) to (11), the beam patterns for Codebooks DB, BD, and DD are calculated as follows:

$$\begin{aligned} &g_{\mathrm{DB},p_a,p_e}(\phi,\theta) \\ &= \frac{1}{Q}\frac{\sin\left\{\frac{\pi Q}{2}\left(\cos\theta\sin\phi+1-\frac{2p_a}{Q}-\frac{2}{Q}\right)\right\}}{\sin\left\{\frac{\pi}{2}\left(\cos\theta\sin\phi+1-\frac{2p_a}{Q}-\frac{2}{Q}\right)\right\}} \\ &\quad\times\frac{\sin\left\{\frac{\pi Q}{2}\left(\sin\theta+1-\frac{2p_e}{Q}-\frac{1}{Q}\right)\right\}}{\sin\left\{\frac{\pi}{2}\left(\sin\theta+1-\frac{2p_e}{Q}-\frac{1}{Q}\right)\right\}} \\ &\quad\times\exp\left\{j\left(Q-1\right)\frac{D_{p_a}+B_{p_e}}{2}\right\} \end{aligned} \tag{12}$$

where

$$D_{p_a} = \pi\left(\cos\theta\sin\phi+1-\frac{2p_a}{Q}-\frac{2}{Q}\right) \tag{13}$$

$$\begin{aligned} &g_{\mathrm{BD},p_a,p_e}(\phi,\theta) \\ &= \frac{1}{Q}\frac{\sin\left\{\frac{\pi Q}{2}\left(\cos\theta\sin\phi+1-\frac{2p_a}{Q}-\frac{1}{Q}\right)\right\}}{\sin\left\{\frac{\pi}{2}\left(\cos\theta\sin\phi+1-\frac{2p_a}{Q}-\frac{1}{Q}\right)\right\}} \\ &\quad\times\frac{\sin\left\{\frac{\pi Q}{2}\left(\sin\theta+1-\frac{2p_e}{Q}-\frac{2}{Q}\right)\right\}}{\sin\left\{\frac{\pi}{2}\left(\sin\theta+1-\frac{2p_e}{Q}-\frac{2}{Q}\right)\right\}} \\ &\quad\times\exp\left\{j\left(Q-1\right)\frac{B_{p_a}+D_{p_e}}{2}\right\} \end{aligned} \tag{14}$$

where

$$D_{p_e} = \pi\left(\sin\theta+1-\frac{2p_e}{Q}-\frac{2}{Q}\right) \tag{15}$$

$$\begin{aligned} &g_{\mathrm{DD},p_a,p_e}(\phi,\theta) \\ &= \frac{1}{Q}\frac{\sin\left\{\frac{\pi Q}{2}\left(\cos\theta\sin\phi+1-\frac{2p_a}{Q}-\frac{2}{Q}\right)\right\}}{\sin\left\{\frac{\pi}{2}\left(\cos\theta\sin\phi+1-\frac{2p_a}{Q}-\frac{2}{Q}\right)\right\}} \\ &\quad\times\frac{\sin\left\{\frac{\pi Q}{2}\left(\sin\theta+1-\frac{2p_e}{Q}-\frac{2}{Q}\right)\right\}}{\sin\left\{\frac{\pi}{2}\left(\sin\theta+1-\frac{2p_e}{Q}-\frac{2}{Q}\right)\right\}} \\ &\quad\times\exp\left\{j\left(Q-1\right)\frac{D_{p_a}+D_{p_e}}{2}\right\} \end{aligned} \tag{16}$$

For the sake of simple expression, we write the four beam patterns by single notation as

$$g_{\mathrm{R},p_a,p_e}(\phi,\theta), \tag{17}$$

where R is one of BB, DB, BD, DD depending on the corresponding codebook. Furthermore, we call $\mathrm{R}, p_a.p_e$ a beam pattern index.

The beam patterns in the azimuth domain are shown in Fig. 9 for codebooks BB and DB, where $Q = 8$ and elevation angle $-7.2°$ ($p_e = 3$). The angle $-7.2°$ is the peak elevation angle of the beam pattern formed by the Butler matrix when $Q = 8$ and $p_e = 3$. This is obtained by solving the following equation for $\theta$

$$\sin\theta + 1 - \frac{2p_e}{Q} - \frac{1}{Q} = 0. \tag{18}$$

This equation has been derived from (6) or (12).

Since we have 64 elements, the maximum gain is 18 dB. From the figures, we see that the gain at angles where two beams cross each other is about 14 dB. This means that if we use a single codebook, we have about 4 dB degradation in the worst case. Furthermore, it is seen that beams of one codebook have the maximum gain around angles where beams of the other codebook have the lowest value, and that beams of both codebooks help each other. The degradation is reduced to about 1 dB. This is the reason why we use both the Butler matrix and DFT matrix codebooks. We have stated the azimuth case so far, and the situation is the same also for the elevation. Thus, we have BB, DB, BD, DD in all. The four codebooks improve the performance comparing with the single codebook BB. In the next subsection, it will be shown that the performance of the four codebooks is much better than that of the single codebook BB.

Now, we explain the IRS control in more detail. The BS sends pilot symbols. Each symbol has $L$-equal-amplitude components at equal frequency intervals in a communication

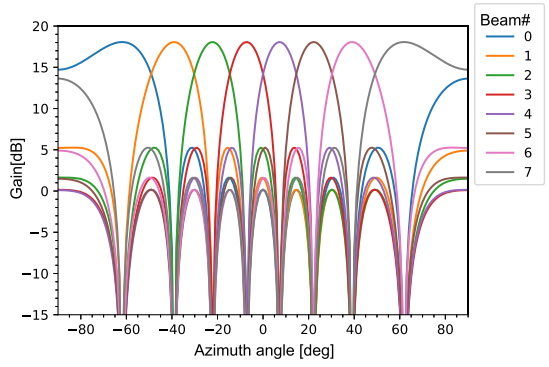


(a) Codebook BB.

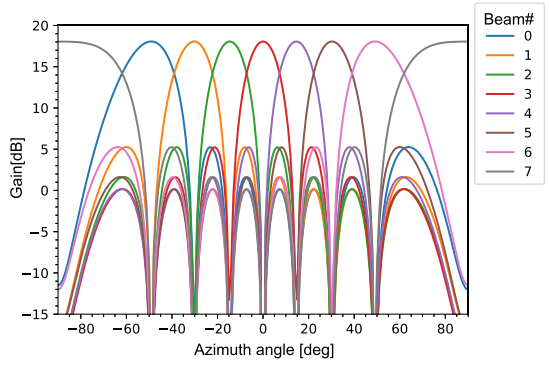


(b) Codebook DB.

**Fig. 9** Beam patterns in the azimuth domain for codebooks BB and DB. $Q = 8$ and elevation angle $-7.2°$ ($p_e = 3$).

band. For example, each pilot symbol has equal-amplitude components at $L$ frequency points such as 140.0 GHz, 140.1 GHz, 140.2 GHz, $\cdots$. The IRS reflects the pilot symbols changing the beam patterns. For simplicity, the incident power to the IRS is normalized to 1. We assume that we have $I$ TCs, and the $i$th TC has $K_i$ SPs between the IRS and UE. For the beam pattern index $R, p_a, p_e$, the complex amplitude $B_{\mathrm{R},p_a.p_e,i,k,l}$ of the pilot received by the UE via the $k$th SP within the $i$th TC at frequency $f_l$ is expressed as

$$B_{\mathrm{R},p_a,p_e,i,k,l} = A_{i,k}\exp(j\beta_{i,k})g_{\mathrm{R},p_a,p_e}(\phi_{i,k},\theta_{i,k})\exp(-j2\pi f_l\tau_{i,k}), \quad (19)$$

where $A_{i,k}, \beta_{i,k}, \phi_{i,k}, \theta_{i,k}, \tau_{i,k}$ denote the amplitude, phase, AOD, EOD, and delay of the $k$th SP within the $i$th TC, respectively. It should be noted that the actual complex amplitude is given by multiplying the righthand side of (19) by $\sqrt{\frac{P_r}{L}}$, where $P_r$ denotes the total received omnidirectional power [41]. However, $P_r$ does not affect the IRS control, and we have omitted $\sqrt{\frac{P_r}{L}}$ in (19). The pilot symbol power of the total $L$ frequency points observed at the UE is given by

$$P_{\mathrm{R},p_a,p_e} = \sum_{l=0}^{L}\left|\sum_{i=1}^{I}\sum_{k=1}^{K_i}B_{\mathrm{R},p_a,p_e,i,k,l}\right|^2. \quad (20)$$

We choose the beam pattern index R, $p_a$, $p_e$ that maximizes (20). The reason why we use $L$ frequency points is because we want to choose the beam pattern index that maximizes the average power in frequency-selective fading environments due to multipath delay. We represent the optimum beam pattern as $g_{\mathrm{opt}}(\phi,\theta)$, and the corresponding $Q \times Q$ complex weights as $w'_{\mathrm{opt},q_y,q_z}$, which are given by one of (1), (9), (10), and (11). The UE informs the BS of the chosen beam pattern, and the BS controls the phases of IRS. Concretely, the BS applies the phases of the complex weights $w'_{\mathrm{opt},q_y,q_z}$ to the phase-shift devices of the IRS elements in Fig. 8. This is one of SRE cases shown in Fig. 1(b).

To evaluate the performance of the chosen beam pattern index R, $p_a$, $p_e$, we introduce average power $P_{\mathrm{av}}$ over $M$ frequency points in the band, which is defined as

$$P_{\mathrm{av}} = \frac{1}{M}\sum_{m=1}^{M}\left|\sum_{i=1}^{I}\sum_{k=1}^{K_i}A_{i,k}g_{\mathrm{opt}}(\phi_{i,k},\theta_{i,k})\exp(-j2\pi f_m\tau_{i,k}+\beta_{i,k})\right|^2. \quad (21)$$

$M$ is so large that $P_{\mathrm{av}}$ gives an approximate average power over the communication band, and $M \gg L$ holds. If we obtain the cumulative distribution function changing $\phi_{i,k}$, $\theta_{i,k}$, and $\beta_{i,k}$, we can evaluate the IRS control method performance, which will be shown in the next subsection.

It is easily seen that when we have a single dominant path between the IRS and UE, the method based on beamforming works very well. Conversely, when we have many multipath components, the performance degrades because much of power outside the chosen beam is not used for transmission. As stated in Sect. 3, we have only a few multipath components in sub-Terahertz bands, and we can expect the method works well.

We have four codebooks, and each codebook has $Q^2$ beams. In total, we have $4Q^2$ candidates for the IRS optimization. In this paper, we examine all of them to obtain the optimum beam. This is an exhaustive search. When $Q$ is large, the optimization process takes a long time. We have, however, techniques to reduce the overhead such as a multi-stage beamforming codebook or a hierarchical codebook [43]–[45]. We can say that we have techniques to reduce the beam searching time. Detail considerations on this issue for the communication system with the IRS is future work.

To evaluate the IRS control based on beamforming, we derive the upper bound of the average power given by (21). The channel at frequency $f_m$ between the element $(q_y, q_z)$ of the IRS and the UE is given by

$$h_{m,q_y,q_z} = \sum_{i=1}^{I}\sum_{k=1}^{K_i}A_{i,k}\exp(j\beta_{i,k})\exp(-j2\pi f_m\tau_{i,k}) \exp\{j\pi(q_y\cos\theta_{i,k}\sin\phi_{i,k} + q_z\sin\theta_{i,k})\}. \quad (22)$$

The optimum complex weights add all the radio waves in phase at the UE, and are given by

$$w_{\mathrm{opt},m,q_y,q_z} = \frac{h^*_{m,q_y,q_z}}{Q|h_{m,q_y,q_z}|}, \tag{23}$$

where * denotes the complex conjugate. The reason why $Q$ is included in the denominator is because we need to make the radiated power equal to the input power, which is the same as the case of (1). When we optimize the IRS using (23), we obtain the upper bound $P_{\mathrm{ub}}$ as follows:

$$\begin{aligned} P_{\mathrm{ub}} &= \frac{1}{M}\sum_{m=1}^{M}\left|\sum_{q_y=1}^{Q}\sum_{q_z=1}^{Q} w_{\mathrm{opt},m,q_y,q_z} h_{m,q_y,q_z}\right|^2 \\ &= \frac{1}{M}\sum_{m=1}^{M}\left(\frac{\sum_{q_y=1}^{Q}\sum_{q_z=1}^{Q}|h_{m,q_y,q_z}|}{Q}\right)^2 \end{aligned} \tag{24}$$

In the next subsection, we compare the average power $P_{\mathrm{av}}$ with (24) for several propagation environments.

### 4.2 Simulations

We evaluated the performance of the IRS based mainly on the channel model proposed in [27], [41]. The simulation parameters are listed in Table 2. We examined three cases of multipath propagation as shown in Tables 3, 4, and 5, where the number of multipath components is 1, 3, and 6, respectively. "Delay" represents the excess delay for (TC#$i$, SP#$k$) with respect to (TC#1, SP#1), which is the direct path from the IRS to the UE. "Power" for (TC#$i$, SP#$k$) was calculated using "Delay." Note that the total of "Power" is normalized to 1 for each case. "Amplitude $A_{i,k}$" is the square root of "Power." The phase $\beta_{i,k}$ was determined by a uniform random number (URN) $[0, 2\pi]$ for each trial, and was used in (19), (21) and (22).

**Table 2** Simulation parameters.

| | |
|---|---|
| Frequency range [GHz] | 140~141 |
| Number of IRS elements, $Q \times Q$ | $8 \times 8$ |
| Number of frequency points in each pilot symbol, $L$ | 11 |
| Number of frequency points for averaging, $M$ | 1001 |
| Number of trails | 1000 |

The AODs and EODs were obtained in the following way. Main directions of departure are called spatial lobes (SLs). The 1-path case in Table 3 has a single SL, and the 3-path case in Table 4 has two SLs. Multiple TCs can arrive at unique pointing angles [41]. The Ref. [27] states that there are at most two SLs at 140 GHz in the measurement environment. Thus, even when there are three TCs, the number of SLs is one or two. The 6-path case in Table 5 has three TCs and two SLs. We represent the mean AOD and EOD for SL#$n$ by $\Phi_n$ and $\Theta_n$, respectively. As shown in Tables 3, 4, and 5, the AOD and EOD of (TC#$i$, SP#$k$) are given by the sum of the means and deviations $(\Delta\Phi_n)_{i,k}$ and $(\Delta\Theta_n)_{i,k}$ except the direct path (TC#1, SP#1). The direct path is determined by the positions of the IRS and the UE, we do not need to add the deviations.

The means and deviations are determined by random numbers as follows:

$\Phi_1$: URN $[-75$ deg, $-45$ deg$]$

$\Theta_1$: URN $[-10$ deg, $-5$ deg$]$

$\Phi_2$: URN [15 deg, 45 deg]

$\Theta_2$: Normal random number (NRN) with mean $-6.8$ deg and standard deviation 4.9 deg

$(\Delta\Phi_n)_{i,k}, n = 1, 2, i = 1, 2, 3, k = 1, 2$: Independent NRNs with mean 0 deg and standard deviation 4.3 deg

$(\Delta\Theta_n)_{i,k}, n = 1, 2, i = 1, 2, 3, k = 1, 2$: Independent NRNs with mean 0 deg and standard deviation 3.4 deg

Here, we explain the reason why we used those random numbers.

$\Phi_1$ is the AOD of the direct path from the IRS, that is, the azimuth direction to the UE. As shown in Fig. 7(a), the UE is located in the NLOS region of the BS due to the obstacle. $\Phi_1$ given by URN $[-75$ deg, $-45$ deg$]$ is consistent with this.

**Table 3** Multipath parameters for a 1-path case.

| TC#$i$ | SP#$k$ | Delay [ns] | Power | Amplitude $A_{i,k}$ | AOD | EOD |
|---|---|---|---|---|---|---|
| 1 | 1 | 0 | 1.0 | 1.0 | $\phi_{1,1} = \Phi_1$ | $\theta_{1,1} = \Theta_1$ |

**Table 4** Multipath parameters for a 3-path case.

| TC#$i$ | SP#$k$ | Delay [ns] | Power | Amplitude $A_{i,k}$ | AOD | EOD |
|---|---|---|---|---|---|---|
| 1 | 1 | 0 | 0.5950 | 0.7714 | $\phi_{1,1} = \Phi_1$ | $\theta_{1,1} = \Theta_1$ |
| 2 | 1 | 7.0 | 0.2521 | 0.5021 | $\phi_{2,1} = \Phi_2 + (\Delta\Phi_2)_{2,1}$ | $\theta_{2,1} = \Theta_2 + (\Delta\Theta_2)_{2,1}$ |
| | 2 | 8.0 | 0.1529 | 0.3910 | $\phi_{2,2} = \Phi_2 + (\Delta\Phi_2)_{2,2}$ | $\theta_{2,2} = \Theta_2 + (\Delta\Theta_2)_{2,2}$ |

**Table 5** Multipath parameters for a 6-path case.

| TC#$i$ | SP#$k$ | Delay [ns] | Power | Amplitude $A_{i,k}$ | AOD | EOD |
|---|---|---|---|---|---|---|
| 1 | 1 | 0 | 0.2986 | 0.5464 | $\phi_{1,1} = \Phi_1$ | $\theta_{1,1} = \Theta_1$ |
| | 2 | 1.0 | 0.1811 | 0.4256 | $\phi_{1,2} = \Phi_1 + (\Delta\Phi_1)_{1,2}$ | $\theta_{1,2} = \Theta_1 + (\Delta\Theta_1)_{1,2}$ |
| 2 | 1 | 7.0 | 0.1836 | 0.4285 | $\phi_{2,1} = \Phi_2 + (\Delta\Phi_2)_{2,1}$ | $\theta_{2,1} = \Theta_2 + (\Delta\Theta_2)_{2,1}$ |
| | 2 | 7.5 | 0.1429 | 0.3780 | $\phi_{2,2} = \Phi_2 + (\Delta\Phi_2)_{2,2}$ | $\theta_{2,2} = \Theta_2 + (\Delta\Theta_2)_{2,2}$ |
| 3 | 1 | 16.5 | 0.1316 | 0.3628 | $\phi_{3,1} = \Phi_2 + (\Delta\Phi_2)_{3,1}$ | $\theta_{3,1} = \Theta_2 + (\Delta\Theta_2)_{3,1}$ |
| | 2 | 18.0 | 0.0622 | 0.2494 | $\phi_{3,2} = \Phi_2 + (\Delta\Phi_2)_{3,2}$ | $\theta_{3,2} = \Theta_2 + (\Delta\Theta_2)_{3,2}$ |

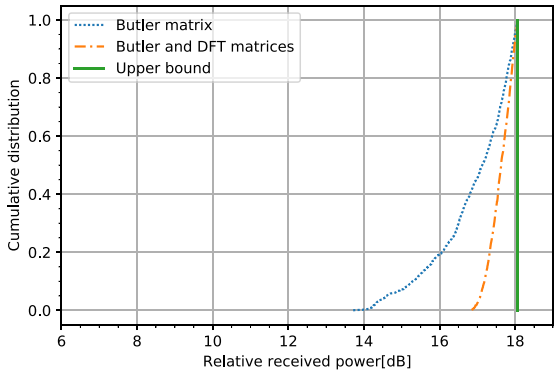


**Fig. 10** Cumulative distributions of relative received power for 1-path case.

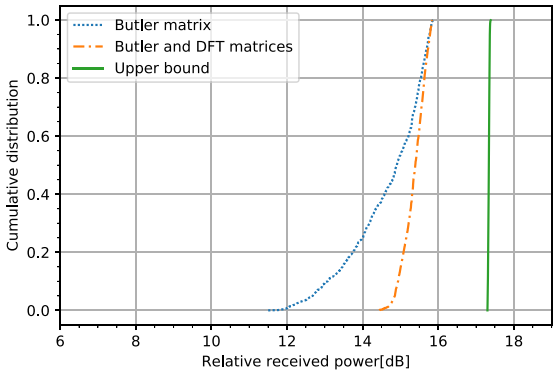


**Fig. 11** Cumulative distributions of relative received power for 3-path case.

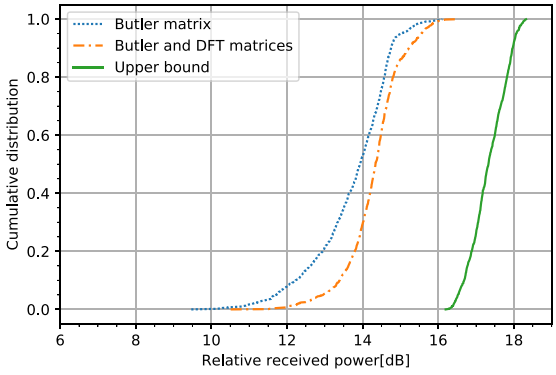


**Fig. 12** Cumulative distributions of relative received power for 6-path case.

$\Theta_1$ is the EOD of the direct path from the IRS, that is, the elevation angle to the UE. In the propagation measurements stated in [27], the TX antenna height was 2.5 m, and the RX one was 1.5 m. According to these settings, we assumed that the heights of the BS and the IRS are 2.5 m from the floor, and that the height of the UE is 1.5 m. We also assumed that the distance between the IRS and the UE is in the range from about 5 m to about 10 m. $\Theta_1$ given by URN [−10 deg, −5 deg] and the above heights meet this distance condition.

$\Phi_2$ is the AOD of SL#2. We assumed that the AOD of SL#2 is far from the UE and also far from the BS. URN [15 deg, 45 deg] satisfies the condition.

$\Theta_2$ is the EOD of SL#2. According to the channel model proposed in [27], the mean EOD is given by NRN with mean −6.8 deg and standard deviation 4.9 deg. As stated above, the heights of the BS and IRS in the simulations are the same as those of the TX and RX in [27]. Then, we used NRN with mean −6.8 deg and standard deviation 4.9 deg for $\Theta_2$.

As for the deviations $(\Delta\Phi_n)_{i,k}$ and $(\Delta\Theta_n)_{i,k}$, we used the same NRNs as those of the channel model in [27].

Now, we present simulation results. We conducted 1000 trials for each case changing the AODs, EODs, and phases $\beta_{i,k}$. Figures 10, 11, and 12 show the cumulative distributions of relative received power for 1-path, 3-path, and 6-path cases, respectively. The legends are defined as follows: "Butler and DFT matrices" is the distribution for the beamforming method using the four codebooks proposed in the previous subsection, namely $P_{\mathrm{av}}$ given by (21);

"Butler matrix" is that using a single codebook BB;

"Upper bound" is the distribution of $P_{\mathrm{ub}}$ given by (24);

Tables 6, 7, and 8 show degradations from the upper bound for the 1-path case, 3-path case, and 6-path case, respectively. They are degradations at 50% and 5% in the cumulative distributions.

We see from Fig. 10 that the proposed method using the four codebooks degrades by only about 1 dB from the upper bound at worst (Butler and DFT matrices). However, if we use only a single codebook BB, the degradation reaches about 4 dB (Butler matrix).

From Figs. 11 and 12, we see that when we have more multipaths, the performance is worse. As stated in the previous subsection, the reason for this is because much of power outside the chosen beam is not used for transmission from the IRS. For the 3-path case, however, the degradations of the proposed four codebook method are only 1.98 dB and 2.56 dB at 50% and 5%, respectively. We think those degradations are small. Even when we have as many as 6 multipath components, the degradation is less than 4 dB. From these results, we can say that the proposed method is useful for

**Table 6** Degradations from the upper bound in the cumulative distributions for the 1-path case.

| | Degradation @ 50% | Degradation @ 5% |
|---|---|---|
| Butler & DFT matrices | 0.46 dB | 0.95 dB |
| Butler matrix | 1.02 dB | 3.62 dB |

**Table 7** Degradations from the upper bound in the cumulative distributions for the 3-path case.

| | Degradation @ 50% | Degradation @ 5% |
|---|---|---|
| Butler & DFT matrices | 1.98 dB | 2.56 dB |
| Butler matrix | 2.49 dB | 4.79 dB |

**Table 8** Degradations from the upper bound in the cumulative distributions for the 6-path case.

| | Degradation @ 50% | Degradation @ 5% |
|---|---|---|
| Butler & DFT matrices | 3.07 dB | 3.73 dB |
| Butler matrix | 3.48 dB | 4.90 dB |

IRS control in sub-Terahertz bands.

## 5. Conclusions

In this paper, we have described SREs for 6G sub-Terahertz-band communications. Sub-Terahertz band waves needed for 6G high-data rate transmission are hard to propagate behind an obstacle due to large diffraction losses. IRSs enable to realize communications overcoming the propagation problem. Since the number of multipath components is small in the band, we have proposed the IRS control based on beamforming, which is realized by phases of a Butler or DFT matrix. This method can avoid difficult channel estimation and phase optimization problems. Simulation results have shown that it reveals good performance in the sense that the received power is not so lower than the upper bound value, especially when the number of multipath components is small. We need to reduce the processing burden to choose an adequate beam, and this is our future work.

### References

[1] Oulu University, "White paper on 6G networking–6G Research Visions," no.6, June 2020. ISBN9789526226842
[2] H. Viswanathan and P.E. Mogensen, "Communications in the 6G era," IEEE Access, vol.8, pp.57063–57074, March 2020. DOI: 10.1109/ACCESS.2020.2981745
[3] M. Giordani, M. Polese, M. Mezzavilla, S. Rangan, and M. Zorzi, "Toward 6G networks: Use cases and technologies," IEEE Commun. Mag., vol.58, no.3, pp.55–61, March 2020. DOI: 10.1109/MCOM.001.1900411
[4] W. Jiang, B. Han, M.A. Habibi, and H.D. Schotten, "The road towards 6G: A comprehensive survey," IEEE Open J. Commun. Soc., vol.2, pp.334–366, Feb. 2021. DOI: 10.1109/OJCOMS.2021.3057679
[5] E. Dahlman, G. Mildh, S. Parkvall, P. Persson, G. Wikström, and H. Mura, "5G evolution and beyond," Trans. IEICE Commun., vol.E104-B, no.9, pp.984–991, Sept. 2021. DOI: 10.1587/transcom.2020FGI0001
[6] I.F. Akyildiz, J.M. Jornet, and C. Han, "Terahertz band: Next frontier for wireless communications," Phys. Commun., vol.12, no.2, pp.16–32, Sept. 2014. DOI: 10.1016/J.PHYCOM.2014.01.006
[7] K. Sengupta, T. Nagatsuma, and D.M. Mittleman, "Terahertz integrated electronic and hybrid electronic-photonic systems," Nature Electron., vol.1, no.12, pp.622–635, Dec. 2018. DOI: 10.1038/s41928-018-0173-2
[8] T. Kawanishi, "THz and photonic seamless communications," IEEE/OSA J. Light. Technol., vol.37, no.7, pp.1671–1679, April 2019. DOI: 10.1109/JLT.2019.2897042
[9] T.S. Rappaport, Y. Xing, O. Kanhere, S. Ju, A. Madanayake, S. Mandal, A. Alkhateeb, and G.C. Trichopoulos, "Wireless communications and applications above 100 GHz: Opportunities and challenges for 6G and beyond," IEEE Access, vol.7, pp.78729–78757, June 2019. DOI: 10.1109/ACCESS.2019.2921522
[10] M. Di Renzo, A. Zappone, M. Debbah, M.-S. Alouini, C. Yuen, J. Rosny, and S. Tretyakov, "Smart radio environments empowered by reconfigurable intelligent surfaces: How it works, state of research, and the road ahead," IEEE J. Sel. Areas Commun., vol.38, no.11, pp.2450–2525, Nov. 2020. DOI: 10.1109/JSAC.2020.3007211
[11] C. Liaskos, S. Nie, A. Tsioliaridou, A. Pitsillides, S. Ioannidis, and I. Akyildiz, "A new wireless communication paradigm through software-controlled metasurfaces," IEEE Commun. Mag., vol.56, no.9, pp.162–169, Sept. 2018. DOI: 10.1109/MCOM.2018.1700659
[12] M. Di Renzo, M. Debbah, D.-T. Phan-Huy, A. Zappone, M.-S. Alouini, C. Yuen, V. Sciancalepore, G.C. Alexandropoulos, J. Hoydis, H. Gacanin, J. de Rosny, A. Bounceur, G. Lerosey, and M. Fink, "Smart radio environments empowered by reconfigurable AI meta-surfaces: An idea whose time has come," EURASIP J. Wireless Commun. Netw., vol.2019, no.129, pp.1–20, May 2019. DOI: 10.1186/s13638-019-1438-9
[13] E. Basar, M. Di Renzo, J. de Rosny, M. Debbah, M.-S. Alouini, and R. Zhang, "Wireless communications through reconfigurable intelligent surfaces," IEEE Access, vol.7, pp.116753–116773, Aug. 2019. DOI: 10.1109/ACCESS.2019.2935192
[14] Q. Wu and R. Zhang, "Towards smart and reconfigurable environment: Intelligent reflecting surface aided wireless network," IEEE Commun. Mag., vol.58, no.1, pp.106–112, Jan. 2020. DOI: 10.1109/MCOM.001.1900107
[15] E. Björnson, Ö. Özdogan, and E.G. Larsson, "Reconfigurable intelligent surfaces: Three myths and two critical questions," IEEE Commun. Mag., vol.58, no.12, pp.90–96, Dec. 2020. DOI: 10.1109/MCOM.001.2000407
[16] C. Pan, H. Ren, K. Wang, J.F. Kolb, M. Elkashlan, M. Chen, M. Di Renzo, Y. Hao, J. Wang, A.L. Swindlehurst, X. You, and L. Hanzo, "Reconfigurable intelligent surfaces for 6G systems: Principles, applications, and research directions," IEEE Commun. Mag., vol.59, no.6, pp.14–20, June 2021. DOI: 10.1109/MCOM.001.2001076
[17] Y. Zhu, B. Mao, Y. Kawamoto, and N. Kato, "Intelligent reflecting surface-aided vehicular networks toward 6G: Vision, proposal, and future directions," IEEE Veh. Technol. Mag., vol.16, no.4, pp.48–56, Dec. 2021. DOI: 10.1109/MVT.2021.3113890
[18] R. Liu, Q. Wu, M. Di Renzo, and Y. Yuan, "A path to smart radio environments: An industrial viewpoint on reconfigurable intelligent surfaces," IEEE Wireless Commun., vol.29, no.1, pp.202–208, Feb. 2022. DOI: 10.1109/MWC.111.2100258
[19] E. Björnson, H. Wymeersch, B. Matthiesen, P. Popovski, L. Sanguinetti, and E. de Carvalho, "Reconfigurable intelligent surfaces: A signal processing perspective with wireless applications," IEEE Signal Process. Mag., vol.39, no.2, pp.135–158, March 2022. DOI: 10.1109/MSP.2021.3130549
[20] V. Arun and H. Balakrishnan, "RFocus: Beamforming using thousands of passive antennas," Proc. USENIX Symp. Networked Syst. Design Implement., pp.1047–1061, Feb. 2020.
[21] X. Pei, H. Yin, L. Tan, L. Cao, Z. Li, K. Wang, K. Zhang, and E. Björnson, "RIS-aided wireless communications: Prototyping, adaptive beamforming, and indoor/outdoor field trials," IEEE Trans. Commun., vol.69, no.12, pp.8627–8640, Dec. 2021. DOI: 10.1109/TCOMM.2021.3116151
[22] D. Kitayama, Y. Hama, K. Goto, K. Miyachi, T. Motegi, and O. Kagaya, "Transparent dynamic metasurface for a visually unaffected reconfigurable intelligent surface: Controlling transmission/reflection and making a window into an RF lens," Opt. Express, vol.29, no.18, pp.29292–29307, Aug. 2021. DOI: 10.1364/OE.435648
[23] B. Zheng and R. Zhang, "Intelligent reflecting surface-enhanced OFDM: Channel estimation and reflection optimization," IEEE Wireless Commun. Lett., vol.9, no.4, pp.518–522, April 2020. DOI: 10.1109/LWC.2019.2961357
[24] X. Hou, X. Li, X. Wang, L. Chen, and S. Suyama, "Some observations and thoughts about reconfigurable intelligent surface application for 5G evolution and 6G," ZTE Communications, vol.20, no.1, pp.14–20, March 2022. DOI: 10.12142/ZTECOM.202201003
[25] M. Iwabuchi, T. Murakami, R. Ohmiya, T. Ogawa, Y. Takatori, D. Kitayama, Y. Kishiyama, and T. Asai, "Intelligent radio-wave design: Distributed intelligent reflecting surface with direction-based control for millimeter-wave communications," Proc. 2020 International Conference on Emerging Technologies for Communications (ICETC 2020), IA2-2, Dec. 2020. DOI: 10.34385/proc.63.IA2-2
[26] S.L.H. Nguyen, J. Järveläinen, A. Karttunen, K. Haneda, and

J. Putkonen, "Comparing radio propagation channels between 28 and 140 GHz bands in a shopping mall," 12th European Conference on Antennas and Propagation (EuCAP 2018), April 2018. DOI: 10.1049/cp.2018.0874

[27] S. Ju, Y. Xing, O. Kanhere, and T.S. Rappaport, "Millimeter wave and sub-Terahertz spatial statistical channel model for an indoor office building," IEEE J. Sel. Areas Commun., vol.39, no.6, pp.1561–1575, June 2021. DOI: 10.1109/JSAC.2021.3071844

[28] J. Gomez-Ponce, N.A. Abbasi, A.E. Willner, C.J. Zhang, and A.F. Molisch, "Directionally resolved measurement and modeling of THz band propagation channels," IEEE Open J. Antennas Propag., vol.3, pp.663–686, June 2021. DOI: 10.1109/OJAP.2022.3181326

[29] S. Ju, Y. Xing, O. Kanhere, and T.S. Rappaport, "Sub-terahertz channel measurements and characterization in a factory building," Proc. IEEE Int. Commun. Conf. (ICC), May 2022. DOI: 10.1109/ICC45855.2022.9838910

[30] Press release from NTT DOCOMO on Jan. 24, 2020. https://www.docomo.ne.jp/english/info/media_center/pr/2020/0124_00.html

[31] NTT DOCOMO, "White paper: 5G evolution and 6G (version 5.0)," Jan. 2023. https://www.docomo.ne.jp/english/binary/pdf/corporate/technology/whitepaper_6g/DOCOMO_6G_White_PaperEN_v5.0.pdf

[32] M. Iwabuchi, S. Suyama, T. Arai, M. Nakamura, K. Goto, R. Ohmiya, D. Uchida, T. Yamada, and T. Ogawa, "Concept and issues of new radio network topology for 5G evolution & 6G," IEICE Technical Report, RCS2022-148, Oct. 2022.

[33] S. Suyama, T. Okuyama, Y. Kishiyama, S. Nagata, and T. Asai, "A study on extreme wideband 6G radio access technologies for achieving 100 Gbps data rate in higher frequency bands," IEICE Trans. Commun., vol.E104-B, no.9, pp.992–999, Sept. 2021. DOI: 10.1587/transcom.2020FGI0002

[34] H. Fukuzono, S. Suyama, D. Lee, D. Uchida, T. Okuyama, M. Iwabuchi, J. Mashino, and Y. Kishiyama, "Issues of sub-terahertz-band radio access technologies for 6G," IEICE Technical Report, RCS2021-180, Dec. 2021.

[35] S. Suyama, T. Okuyama, N. Nonaka, and T. Asai, "NTT DOCOMO's activities for utilization of sub-terahertz wave in 6G," IEICE General Conf., CI-7-6, March 2022.

[36] H. Fukuzono, K. Kuriyama, D. Uchida, M. Yoshioka, T. Miyagi, T. Onizawa, S. Suyama, T. Okuyama, and Y. Kishiyama, "Experimental evaluation of LLRs for nonlinearly distorted constellations on single-carrier transmission in a 97 GHz band," IEICE General Conf., B-5-37, March 2022.

[37] S. Suyama, T. Okuyama, N. Nonaka, and T. Asai, "Recent studies on massive MIMO technologies for 5G evolution and 6G," IEEE Radio and Wireless Symposium (RWS), pp.90–93, Jan. 2022. DOI: 10.1109/RWS53089.2022.9719949

[38] Press release from NTT DOCOMO on June 6, 2022. https://www.docomo.ne.jp/english/info/media_center/pr/2022/0606_00.html

[39] M. Nakamura, S. Suyama, K. Kitao, T. Tomie, M. Inomata, W. Yamada, N. Kuno, and M. Sasaki, "Measurement of multipath waves at 160 GHz and 300 GHz in an indoor conference room," EuCAP2023, March 2023.

[40] Beyond 5G Promotion Consortium, "Beyond 5G white paper — Message to the 2030s — (version 1.51)," Oct. 2022. https://b5g.jp/doc/whitepaper_en_1-51.pdf

[41] M.K. Samimi and T.S. Rappaport, "3-D millimeter-wave statistical channel model for 5G wireless system design," IEEE Trans. Microw. Theory Techn., vol.64, no.7, pp.2207–2225, July 2016. DOI: 10.1109/TMTT.2016.2574851

[42] Y. Ogawa, T. Utsuno, T. Nishimura, T. Ohgane, and T. Sato, "Sub-terahertz MIMO spatial multiplexing in indoor propagation environments," IEICE Trans. Commun., vol.E105-B, no.10, pp.1130–1138, Oct. 2022. DOI: 10.1587/transcom.2021MEI0004

[43] L. Chen, Y. Yang, X. Chen, and W. Wang, "Multi-stage beamforming codebook for 60 GHz WPAN," Proc. 6th Int. ICST Conf. Commun. Network. China, pp.361–365, Aug. 2011. DOI: 10.1109/ChinaCom.2011.6158179

[44] A. Alkhateeb, O.E. Ayach, G. Leus, and R.W. Heath, "Channel estimation and hybrid precoding for millimeter wave cellular systems," IEEE J. Sel. Top. Signal Process., vol.8, no.5, pp.831–846, Oct. 2014. DOI: 10.1109/JSTSP.2014.2334278

[45] S. Gao, T. Dong, C. Chen, and Y. Jin, "Hierarchical beam selection in mmWave multiuser MIMO systems with one-bit analog phase shifters," Proc. 2016 8th International Conference on Wireless Communications & Signal Processing (WCSP), Oct. 2016. DOI: 10.1109/WCSP.2016.7752457

**Yasutaka Ogawa** received the B.E., M.E., and Ph.D. degrees from Hokkaido University, Sapporo, Japan, in 1973, 1975, and 1978, respectively. Since 1979, he has been with Hokkaido University, where he is currently a Professor Emeritus. During 1992–1993, he was with ElectroScience Laboratory, the Ohio State University, as a Visiting Scholar, on leave from Hokkaido University. His professional expertise encompasses super-resolution estimation techniques, applications of adaptive antennas for mobile communication, multiple-input multiple-output (MIMO) techniques, and measurement techniques. He proposed a basic and important technique for time-domain super-resolution estimation for electromagnetic wave measurement such as antenna gain measurement, scattering/diffraction measurement, and radar imaging. Also, his expertise and commitment to advancing the development of adaptive antennas contributed to the realization of space division multiple accesses (SDMA) in the Personal Handy-phone System (PHS). He received the Yasujiro Niwa Outstanding Paper Award in 1978, the Young Researchers' Award of IEICE in 1982, the Best Paper Award from IEICE in 2007, TELECOM system technology award from the Telecommunications Advancement Foundation of Japan in 2008, the Best Magazine Paper Award from IEICE Communications Society in 2011, the Achievement Award from IEICE in 2014, and the Best Tutorial Paper Award from IEICE Communications Society in 2018. He also received the Hokkaido University Commendation for excellent teaching in 2012. He is a Life Fellow of the IEEE.

**Shuto Tadokoro** received his B.E. degree in electronics and information engineering from Hokkaido University, Sapporo, Japan, in 2022. He is currently a master course student at the Graduate School of Information Science and Technology, Hokkaido University. His research interests are communication systems using intelligent reflecting surfaces in a sub-Terahertz band.

**Satoshi Suyama** received the B.S. degree in electrical and electronic engineering, the M.S. degree in information processing, and the Dr. Eng. degree in communications and integrated systems, all from Tokyo Institute of Technology, Tokyo, Japan, in 1999, 2001, and 2010, respectively. From 2001 to 2013, he was an Assistant Professor in the Department of Communications and Integrated Systems at the Tokyo Institute of Technology. He has been engaged in research on OFDM mobile communications systems and applications of the adaptive signal processing, including turbo equalization, interference cancellation, and channel estimation. Since April 2013, he has joined NTT DOCOMO, INC. and has been involved in research and development of 5G and 6G mobile communications systems. He is currently Senior Manager of 6G Promotion Department in NTT DOCOMO. He received the Best Paper Prize from the European Wireless Technology Conference (EuWiT) in 2009, the Paper Award from IEICE in 2012, the Best Paper Award from International Symposium on Personal, Indoor and Mobile Radio Communications (PIMRC) in 2016, and the Best Paper Award from IEICE Communications Society in 2022. He is a member of IEICE and IEEE.

**Masashi Iwabuchi** received the B.S. and M.S. degrees from the Tokyo Institute of Technology, Tokyo, Japan, in 2008 and 2010, respectively. From 2010 to 2016, he joined the NTT Access Network Service Systems Laboratories, Nippon Telegraph and Telephone Corporation (NTT). From 2016 to 2019, he was associated with NTT DOCOMO, Inc. Since 2019, he has been with NTT. His current interests are smart repeaters and reconfigurable intelligent surface technologies for 5G evolution and 6G. He is a member of IEICE. He has received the Young Engineers Award from the Institute of Electronics, Information and Communication Engineers (IEICE) in 2015.

**Toshihiko Nishimura** received the B.S. and M.S. degrees in physics and Ph.D. degree in electronics engineering from Hokkaido University, Sapporo, Japan, in 1992, 1994, and 1997, respectively. Since 1998, he has been with Hokkaido University, where he is currently a Professor. His current research interests are in MIMO systems using smart antenna techniques. He received the Young Researchers' Award of IEICE in 2000, the Best Paper Award from IEICE in 2007, and TELECOM System Technology Award from the Telecommunications Advancement Foundation of Japan in 2008, the best magazine paper award from IEICE Communications Society in 2011, and the Best Tutorial Paper Award from the IEICE Communications Society in 2018. He is a member of the IEEE.

**Takanori Sato** was born in Hokkaido, Japan, in 1992. He received his Ph.D. degree in the field of media and network technologies from Hokkaido University, Japan, in 2018. He was a Research Fellow of Japan Society for the Promotion of Science (JSPS) from 2017 to 2019. In 2019, he moved to University of Hyogo as an assistant professor. He is currently an associate professor in Hokkaido University. His research interests include the theoretical and numerical studies of optical fibers and photonic circuits using the coupled mode theory and the finite element method. He is a member of the Japan Society of Applied Physics (JSAP), Institute of Electrical and Electronics Engineers (IEEE), and the Optical Society of America (OSA).

**Junichiro Hagiwara** received the B.E., M.E., and Ph.D. degrees from Hokkaido University, Sapporo, Japan, in 1990, 1992, and 2016, respectively. He joined the Nippon Telegraph and Telephone Corporation in April 1992 and transferred to NTT Mobile Communications Network, Inc. (currently NTT DOCOMO, INC.) in July 1992. Later, he became involved in the research and development of mobile communication systems. His current research interests are in the application of stochastic theory to the communication domain. He is currently a visiting professor at Hokkaido University.

**Takeo Ohgane** received the B.E., M.E., and Ph.D. degrees in electronics engineering from Hokkaido University, Sapporo, Japan, in 1984, 1986, and 1994, respectively. From 1986 to 1992, he was with Communications Research Laboratory, Ministry of Posts and Telecommunications. From 1992 to 1995, he was on assignment at ATR Optical and Radio Communications Research Laboratory. Since 1995, he has been with Hokkaido University, where he is currently a Professor. During 2005–2006, he was at Centre for Communications Research, University of Bristol, U.K., as a Visiting Fellow. His research interests are in MIMO signal processing for wireless communications. He received the IEEE AP-S Tokyo Chapter Young Engineer Award in 1993, the Young Researchers' Award of IEICE in 1990, the Best Paper Award from IEICE in 2007, TELECOM System Technology Award from the Telecommunications Advancement Foundation of Japan in 2008, the Best Magazine Paper Award from IEICE Communications Society in 2011, and the Best Tutorial Paper Award from IEICE Communications Society in 2018. He is a member of the IEEE.